Nanoscale

Accepted Manuscript

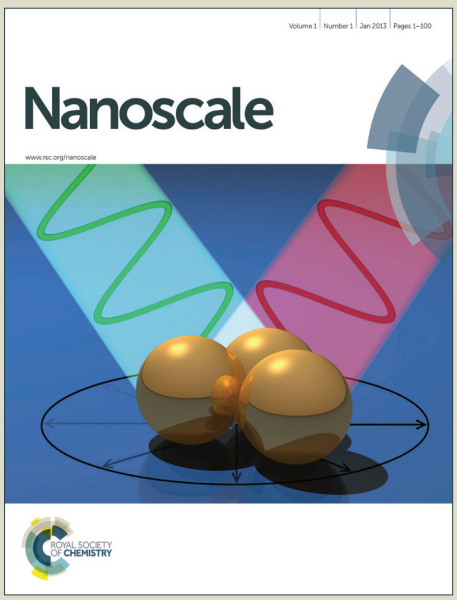

ROYAL SOCIETY OF CHEMISTRY

www.rsc.org/nanoscale

Catalyst Engineering for Lithium Ion Batteries: The Catalytic Role of Ge for Enhancing Electrochemical Performance of $SnO_2(GeO_2)_{0.13}$/G Anodes

Yun Guang Zhu[†,1], *Ye Wang*[†,1], *Zhao Jun Han*[2], *Yumeng Shi*[1], *Jen It Wong*[1], *Zhi Xiang Huang*[1], *Kostya (Ken) Ostrikov,* [2,3,4,5] *Hui Ying Yang*[1]*

[1] Pillar of Engineering Product Development, Singapore University of Technology and Design, 20 Dover Drive, Singapore 138682

[2] CSIRO Manufacturing Flagship, P.O. Box 218, Lindfield, New South Wales 2070, Australia

[3] School of Chemistry, Physics, and Mechanical Engineering, Queensland University of Technology, Brisbane, QLD 4000, Australia

[4] School of Physics, The University of Sydney, New South Wales 2006, Australia

[5] Australian Institute for Innovative Materials, The University of Wollongong, New South Wales 2522, Australia

†These two authors contributed equally to this work.

[*] To whom correspondence should be addressed. E-mail: yanghuiying@sutd.edu.sg

Abstract

The catalytic role of germanium (Ge) was investigated to improve the electrochemical performance of tin dioxide grown on graphene (SnO_2/G) nanocomposites as an anode material of lithium ion batteries (LIBs). Germanium dioxide (GeO_2) and SnO_2 nanoparticles (<10 nm) were uniformly anchored on the graphene sheets via a simple single-step hydrothermal method. The synthesized $SnO_2(GeO_2)_{0.13}$/G nanocomposites can deliver a capacity of 1200 mAh/g at a current density of 100 mA/g, which is much higher than the traditional theoretical specific capacity of such nanocomposites (~702 mAh/g). More importantly, the $SnO_2(GeO_2)_{0.13}$/G nanocomposites exhibited improved rate and large current capability (885 mAh/g at a discharge current of 2000 mA/g) and excellent long cycling stability (almost 100% retention after 600 cycles). The enhanced electrochemical performance was attributed to the catalytic effect of Ge which enabled the reversible reaction of metals (Sn and Ge) to metals oxide (SnO_2 and GeO_2) during the charge/discharge processes. Our demonstrated approach towards nanocomposite catalyst engineering opens new avenues for next-generation high-performance rechargeable Li-ion batteries anode materials.

Keywords: Tin Oxide, Germanium Oxide, Graphene, Catalyst, Lithium Ion Batteries.

1. Introduction

To fulfill the increasing demand of energy storage devices with high energy and power densities, lithium ion batteries (LIBs) are considered as one of the most promising candidates.[1-5] However, commercial graphite-based anode materials for the current LIBs suffer from a relatively low specific capacity (372 mAh/g), which severely hampers their implementations in applications such as portable electronics and grid-level energy storage systems.[6] To tackle this challenge, new and high-performance anode materials have recently been intensively investigated, which mainly include the three-dimensional (3D) transition metal oxides and the alloying-dealloying type materials.[5, 7-14]

As an important alloying-dealloying type anode material, tin oxide (SnO_2) is regarded as one of the most promising anode materials with potentials in commercialization due to its high theoretical capacity (~782 mAh/g), relatively low charge-discharge potential, high abundance, and low cost.[14] However, the performance of SnO_2 anodes remains inferior due to: (i) a huge volume change (259%) during the alloying and dealloying process, which results in fast capacity fading during the cycle process and may lead to severe electrode pulverization; (ii) a low electrical conductivity for the pristine SnO_2 which limits the electron transport and power density; (iii) a low initial Coulombic efficiency (CE) due to the irreversible conversion reaction.[15] Issues (i) and (ii) could be partially resolved by designing new nanostructures (e.g., nanoparticles, nanorods, nanowires, hollow nanospheres, porous microboxes)[16-24] and the incorporation of carbonaceous materials (e.g., carbon nanotubes, graphene oxide, onion-like carbon).[25-29]

Issue (iii) is essentially due to the chemical reactions of the conversion process of SnO_2 to Sn and the subsequent alloying-dealloying process, as given by:

$$SnO_2 + 4\,Li^+ + 4e^- \rightarrow Sn + 2Li_2O \qquad (1)$$

$$Sn + xLi^+ + xe^- \leftrightarrow Li_xSn\ (0 \leq x \leq 4.4) \qquad (2)$$

It generally accepted that the first conversion reaction (eq. 1) is irreversible, leading to a low initial CE. From eq. 2, maximum 4.4 Li-ions can be alloyed with 1 Sn atoms; however, 4 of them are consumed during the first discharge process and become inactivated for the following charge/discharge cycles. If the conversion reaction (eq. 1) is reversible, the theoretic specific capacity can be improved from 782 to 1493 mAh/g due to overall 8.4 Li^+ involved during charge and discharge processes, which has been stated in the supporting information.[30] Indeed, it has recently been reported that the measured SnO_2 specific capacity was higher than the theoretical value, and the improvement was possible attributed to the reversible conversion of Sn to SnO_2.[31] However, the detailed study of such mechanism is still unclear.

Kim et al. reported the nano-sized metallic Cu particles contacted with the nano-sized Ge and Li_2O to catalyze Li_2O decomposition and provide an electronic conductive network for Ge oxidation.[32] Ge was also used as a catalyst to enhance the GeO_2/C nanocomposite electrochemical performance as reported by Seng et al.[33] In this work, Ge is engineered to act as the catalyst for promoting the reversible reaction of Sn into SnO_2, leading to an enhanced electrochemical performance. Since nano-sized Ge is easily oxidized, GeO_2 nanoparticles are used instead of Ge. Meanwhile, reduced graphene oxide (RGO) is employed as a conductive buffer template for accommodating the volume change of the hybrid nanocomposites. In addition, RGO also prevents the aggregation of the nanoparticles. The designed hybrid $SnO_2(GeO_2)_{0.13}$/G electrode not only delivers a capacity beyond its traditional theoretical value (i.e., 702 mAh/g), but also exhibits excellent rate capability (980 and 885 mAh/g at discharge current densities of

1000 and 2000 mA/g, respectively) and ultrahigh stability even at high current densities of 2000 mA/g (almost 100% retention after 600 cycles). For the specific weight capacity of $SnO_2(GeO_2)_{0.13}$/G nanocomposites was calculated in the supporting information.

2. Results and discussion

2.1. Characterization of the Materials

In the preparation process, $SnCl_2$, GeO_2 and GO were dispersed in deionized water and then the solution was transported into an autoclave for hydrothermal reaction. After reaction, the black precipitation ($SnO_2(GeO_2)_{0.13}$/G) was obtained. The morphology of the $SnO_2(GeO_2)_{0.13}$/G and SnO_2/G nanocomposites is shown in Figure 1. One can see that the folded graphene sheets formed an ideal 3D matrix as the soft template for SnO_2 and GeO_2 nanoparticles (Figure 1a). Such a designed material morphology can effectively prevent aggregation of nanoparticles and facilitate the electrolyte penetration into the microstructure of the composites to enhance the electrolyte ion accessibility. More detailed structural analysis was performed by transmission electron microscopy (TEM), as shown in Figures 1b and 1c. It is clearly observed that SnO_2 and GeO_2 nanoparticles with the diameter ranging from 5 to 10 nm uniformly anchored on the graphene sheets. From the selected-area electron diffraction (SAED) pattern (inset of Figure 1b), the multiple diffraction rings indicate that the nanoparticles are nanocrystalline. The corresponding crystalline planes could also be indexed, such as the (100) plane of GeO_2, the expanded (002) plane of graphene, the (110) plane of GeO_2 and/or the (101) plane of SnO_2, as shown in the inset of Figure 1b. In addition, the fringes attributed to the graphene sheet are also identified in Figure 1c. The lattice spacings obtained from the well-resolved lattice fringes of nanoparticles in Figure 1b are 0.33 and 0.34 nm, corresponding to the (110) plane of the tetragonal rutile-like SnO_2 and/or the (101) plane of GeO_2. As shown in Figures 1d and 1e, the

morphology of SnO_2/G is almost the same as that of $SnO_2(GeO_2)_{0.13}$/G nanocomposite. The high-resolution TEM image of SnO_2/G nanocomposites shown in Figure 1f indicated the lattice spacings of 0.33 and 0.26 nm, which are attributed to the (110) and (101) crystal planes of SnO_2, respectively. Typical morphologies of commercial SnO_2 and GeO_2 powders are also shown in Figures S1a and S1b. As one can see, the sizes of commercial SnO_2 or GeO_2 particles are much larger than that of the synthesized nanocomposites. Moreover, the commercial particles are heavily aggregated together.

Figure 2a compares the X-ray diffraction (XRD) patterns of SnO_2/G and $SnO_2(GeO_2)_{0.13}$-G nanocomposites. A broad peak at around 26^o is assigned to the overlap of the (002) plane of graphene and the (110) plane of SnO_2 and/or the (101) plane of GeO_2. The strong characteristic peaks in both nanocomposites correspond to the tetragonal structure of SnO_2 (JCPDS No. 41-1445). Other weak peaks found in $SnO_2(GeO_2)_{0.13}$/G can be indexed to the hexagonal structure of GeO_2 (JCPDS No. 36-1463). The peaks associated with GeO_2 are weak, indicating that the content of GeO_2 in the hybrid nanocomposites is low. Raman spectra of reduced graphene oxide (RGO), SnO_2/G and $SnO_2(GeO_2)_{0.13}$/G nanocomposites are shown in Figure 2b. The peaks centered at 1360 cm^{-1} are the D-peak arising from the defects and disorders in the hexagonal graphitic networks, and the peaks centered at 1570 cm^{-1} is the G-peak due to the vibration of sp^2-bonded carbon atoms in the graphitic lattice.[34] It is generally believed that the intensity ratio between D- and G-peaks (I_D/I_G) indicates the crystal quality of carbon nanostructures. The I_D/I_G is increased from 0.90 to 1.21 and 1.39 for GO, SnO_2/G and $SnO_2(GeO_2)_{0.13}$/G nanocomposites, respectively, indicating the graphene oxide became more defects and disorders after reducing. The graphene oxide partially disrupted after the incorporation of SnO_2 and $SnO_2(GeO_2)_{0.13}$

during the synthesis process. From TGA curves of Figure S2, the portions of graphene in the $SnO_2(GeO_2)_{0.13}$/G and SnO_2/G are around 21.2 and 16.6 wt%, respectively.

Furthermore, the elemental composition and relative atomic content of the synthesized nanocomposites were studied using X-ray photoelectron spectroscopy (XPS). Figure 3a shows the XPS wide-scan spectra of SnO_2/G and $SnO_2(GeO_2)_{0.13}$/G nanocomposites, indicating the presence of Sn, O, and C elements. Ge 3d band was also observed in the spectra of $SnO_2(GeO_2)_{0.13}$/G nanocomposites. The C 1s spectra of $SnO_2(GeO_2)_{0.13}$/G and SnO_2/G are shown in Figure 3b. After deconvoluting the spectra, both nanocomposites displayed peaks for non-oxygenated C-C (at binding energy of 284.7 eV) and C-OH species (at binding energy of 286.2 eV). It is found that the other peaks belong to C=O and C-OOH of RGO (Figure S3) was greatly reduced after the incorporation of SnO_2 and GeO_2 nanoparticles, suggesting that a better electrical conductivity could be obtained in the nanocomposites. The Sn $3d_{3/2}$ and Sn $3d_{5/2}$ peaks of the nanocomposites centered at binding energies of 495.5 and 487.1 eV, respectively, are shown in Figure 3c. As compared to SnO_2/G, the full-width-at-half-maximum (FWHM) of the Sn 3d peaks for $SnO_2(GeO_2)_{0.13}$/G became slightly broadened, implying that the size of SnO_2 was smaller after the introduction of GeO_2, which was in a good agreement with the microscopic observations (Figures 1c and 1f). In order to confirm the presence of Ge for $SnO_2(GeO_2)_{0.13}$/G nanocomposite, Ge 3d (33.1 eV) state was analyzed in Figure 3d. The atomic ratio of Ge : Sn of about 13% was estimated from the intensity of Sn 3d and Ge 3d peaks, confirming the actual nanocomposite as $SnO_2(GeO_2)_{0.13}$/G. Moreover, the energy dispersive X-ray (EDX) analysis was conducted to map the spatial distribution of various elements. As shown in Figure 3e, four elements of Sn, Ge, C, and O are uniformly dispersed, indicating that Sn and Ge were homogeneously distributed within the graphene networks.

2.2. Electrochemical Testing

The electrochemical performance of $SnO_2(GeO_2)_{0.13}$/G nancomposites was evaluated by assembling the nanocomposites as the working electrode into a half-cell battery with a lithium foil as the counter electrode. The electrochemical processes were investigated through cyclic voltammetry (CV) measurements in the potential range of 0.01 – 3.0 V vs Li^+/Li. From the CV curves of $SnO_2(GeO_2)_{0.13}$/G (Figure 4a), there are two clear peaks (centered at 0.95 and 0.1 V) in the first cathodic sweep. The peak at 0.95 V corresponded to the conversion reaction of SnO_2 (or GeO_2) with the Li^+ ions to Sn (or Ge) and Li_2O (eq. 3),[35]

$$MO_2 + 4\,Li^+ + 4e^- \xrightarrow{\text{discharge (1)}} M + 2Li_2O \qquad (3)$$

where M represents Sn or Ge element. The peak at 0.1 V can be ascribed to the lithium alloying with Sn or Ge to form Li-Sn or Li-Ge alloys (eq. 4),[36]

$$M + xLi^+ + xe^- \xrightarrow{\text{discharge (2)}} Li_xM\ (0 \le x \le 4.4) \qquad (4)$$

On the other hand, there are two broad peaks centered at 0.58 and 1.26 V in the first anodic sweep. The former is commonly attributed to the dealloying reaction of Li-Sn or Li-Ge (eq. 5),[36]

$$Li_xM \xrightarrow{\text{charge (3)}} M + xLi^+ + x\,e^-\ (0 \le x \le 4.4) \qquad (5)$$

while the latter could be attributed to the reaction of Sn or Ge with Li_2O (eq. 6),[37]

$$M + 2Li_2O \xrightarrow{\text{charge (4)}} MO_2 + 4Li^+ + 4e^- \qquad (6)$$

Negligible changes are observed in the following CV curves after the first cycle. The irreversible capacity loss in the first cycle can be attributed to the formation of solid-electrolyte interface

(SEI) layer at the interface of the electrolyte and the electrode, as well as the local structural rearrangement in the $SnO_2(GeO_2)_{0.13}$/G nanocomposite to buffer the stress induced during lithiation/delithiation.[38-39]

The galvanostatic discharging/charging curves of the first 5 cycles of $SnO_2(GeO_2)_{0.13}$/G are shown in the Figure 4b. The $SnO_2(GeO_2)_{0.13}$/G electrode exhibited the capacities of 1408 and 2022 mAh/g for the 1st charge and discharge cycle calculated based on the total mass of $SnO_2(GeO_2)_{0.13}$/G, with an initial CE about 70%. Such capacity loss (30%) of the first cycle is generally attributed to the irreversible formation of the SEI layer on the surface of the nanoparticles and the small portion of irreversible conversion reaction of SnO_2 into Sn (the part of GeO_2 nanoparticles is not in contact with SnO_2 nanoparticles) during the first discharge process. More importantly, the CE was increased to almost 100% for the following cycles. From the Figure S4a, the first 5 cycles of SnO_2/G exhibit similar performance to that of $SnO_2(GeO_2)_{0.13}$/G, which can be attributed to the stabilization contributions from graphene. However, without graphene, SnO_2/GeO_2 composites provided a poor stability in the first 5 cycles, as shown in Figure S4b.

The cycling stability test for $SnO_2(GeO_2)_{0.13}$/G, SnO_2-G and SnO_2/GeO_2 nanocomposites was conducted at a discharge current density of 1000 mA/g after five activation cycles, as shown in Figure 4c. $SnO_2(GeO_2)_{0.13}$/G electrode exhibits excellent stability for 200 cycles with a slight increase at the first few cycles. Specifically, at a high current density of 1000 mA/g, the specific capacity of $SnO_2(GeO_2)_{0.13}$/G was increased from 870 mAh/g to 942 mAh/g after 200 cycles. This behavior is notably different from other metal oxide/carbon hybrids for lithium ion storages, which usually degrade to less than 600 mAh/g after 100-200 cycles regardless of a similar high specific capacity at the initial cycles.[35, 40] The increased capacity may be attributed to the delayed

infiltration of the electrolyte into the nanohybrids, the stable structure which prevents pulverization during cycling, and the reversible reaction of metal atoms (Sn and Ge) to metal oxides (SnO_2 and GeO_2). In contrast, the cycling stability of both SnO_2-G and SnO_2/GeO_2 is inferior as expected; for instance, the specific capacity of the SnO_2-G electrode reduces from 990 to 376 mAh/g after 80 cycles, while the SnO_2/GeO_2 nanocomposite nearly completely loses its activity after 40 cycles (Figure 4c).

Figure 4d shows the rate capabilities of the above three electrodes. The $SnO_2(GeO_2)_{0.13}$-G electrode can deliver specific capacities of 1350, 1190, 1120, 1070, 1000, and 900 mAh/g at the current densities of 50, 100, 200, 500, 1000 and 2000 mA/g, respectively. Moreover, the value recovers to about 1200 mAh/g when the current density is returned to 100 mA/g, indicating an excellent reversibility. In contrast, the SnO_2-G electrode displayed rapid capacity fading when the current density was increased higher than 500 mA/g. For the SnO_2/GeO_2 nanocomposites, the specific capacities at both low and high current density exhibited too lower than the other two nanocomposite with graphene. Thus, the presence of graphene could enhance the rate capability for these nanocomposite.

From the above results, one can be seen that the graphene template also played a critical role in achieving the high rate capability of the $SnO_2(GeO_2)_{0.13}$/G nanocomposite. Without graphene, SnO_2/GeO_2 nanocomposite becomes unstable with the increase of the current density, which is possibly due to the pulverization and lose contact with the current collector during lithiation/delithiation. The high rate capability of $SnO_2(GeO_2)_{0.13}$/G at the high current density can be attributed to the interactions between graphene and SnO_2 or GeO_2 nanoparticles, which facilitate effective electron transport between metal oxide nanoparticles and the current collector through the highly-conductive two-dimensional structure.

The electrochemical impedance spectroscopy (EIS) measurements were conducted to investigate the intrinsic electrochemical and kinetic mechanisms of the electrodes, as shown by the Nyquist plots in Figure 5a. It can be seen that the radius of the semicircles $SnO_2(GeO_2)_{0.13}$/G<SnO_2/G<SnO_2/GeO_2, which indicated that $SnO_2(GeO_2)_{0.13}$/G have the best charge transfer among the three composites. With the increased cycles, the radius of the semicircle of SnO_2-G and SnO_2/GeO_2 is increased significantly after 100 cycles (Figure S5), indicating that the SEI film grew thicker with the cycling due to the deposition of amorphous Li_2O matrix and the electrolyte, as well as the unstable structure of the electrode during cycling.[41-42] In contrast, the semicircles in the $SnGe_{0.13}O_{2.26}$-G electrode remained almost unchanged after 100 even until 200 cycles (Figure 5b), indicating that the SEI formation and the composite structure remained stable during the long cycling process.

Finally, the ultra-high stability cycling performance of $SnO_2(GeO_2)_{0.13}$/G nanocomposite was measured at a discharge current density of 2000 mA/g, as shown in Figure 5c. The specific capacity retains almost 100% after 600 cycles and the CE remains near 100% after the first five lithiation/delithiation cycles. This exceptional stability can be attributed to the unique and advantageous features of the $SnO_2(GeO_2)_{0.13}$/G nanocomposites system. First, the effective binding between the uniformly distributed SnO_2 and GeO_2 nanoparticles with the graphene network maintained efficient electron and ion transport during the conversion reactions.[35] Second, the hybrid nanostructure helped to well accommodate the huge volume change of the SnO_2 and GeO_2 during lithiation/delithiation to reduce the cycling degradation. Third, the small particle size and uniform distribution of $SnO_2(GeO_2)_{0.13}$ on the graphene matrix can greatly improve the physical connection and electrical contact with the 2D conductive framework, thereby maximizing the effective electrochemical utilization of the active materials and ensuring a

reversible lithium insertion/extraction process even under high current density.[43] Fourth, the conductive graphene matrix is favorable to form a stable SEI layer and protect the electrolyte from further decomposition while still allow for Li ion transport into the encapsulated SnO_2 and GeO_2 nanoparticles.[35] Lastly, GeO_2 played a key role in catalyzing the reversible reaction of Sn into SnO_2 with an enhanced specific capacity.

As the specific capacity (1200 mAh/g at a current density of 100 mA/g) of the $SnO_2(GeO_2)_{0.13}$/G nanocomposites is much higher than the traditional theoretical value of 702 mA/g given by eq. 4, the most plausible reason for such excessive capacity is from the irreversible reaction based on eq. 3. In other words, the reaction from SnO_2 to Sn became reversible with the assistance of GeO_2, which has been reported to have catalytic effect for the reversible reaction of formation of Ge-O bonds.[32-33] As such, the specific capacity was greatly enhanced due to the conversion from Sn into SnO_2 nanoparticles during the charging process as shown in eq. 6. In addition, graphene sheets provide stable conductive reaction sites to firmly hold and support Ge promote the catalytic reaction of SnO_2, resulting in ultra-high specific capacity, cycling stability and rate performance. Therefore, the synthesized $SnO_2(GeO_2)_{0.13}$/G nanocomposites can deliver a capacity is 93.5% of the theoretical specific capacity (1283 mAh/g) with the irreversible reactions.

2.3. Exploration of the catalytic role of Ge during the cycling process

We illustrate the proposed reaction mechanism of the $SnO_2(GeO_2)_{0.13}$/G nanocomposites during the charge and discharge processes in Figure 6a. Firstly, the SnO_2 and GeO_2 nanoparticles anchored on the graphene sheets are reduced to Sn and Ge, respectively, while Li_2O is accumulated at the interface and gradually covers the nanoparticles during the 1st discharge

process. In the subsequent discharge process, Li ions penetrate into the film of Li_2O and react with Sn and Ge to form Li_xSn and Li_xGe alloys, respectively ($0 \leqslant x \leqslant 4.4$). During this stage, the force associated with the huge volume change leads to nanoparticle fragmentation into smaller ones. The cracked nanoparticles are still held by the graphene sheets. In the following charge process, the alloyed nanoparticles (Li_xSn and Li_xGe ($0 \leqslant x \leqslant 4.4$)) are decomposed into Li^+ and Sn or Ge metal nanoparticles. Due to the catalytic effect of Ge, Sn and Ge will react with Li_2O to form SnO_2 and GeO_2, as shown in eq. 6 (stage 4 in Figure 6). In Figure 6b, the four plateaus corresponding to the above four reactions steps almost overlap with each other after 10, 200, and 400 cycles. In other word, the four electrochemical reactions are very stable with the increase of cycling number. In contrast, the reaction plateaus of SnO_2 or GeO_2 for the SnO_2/GeO_2 and SnO_2/G nanocomposites become shorter with the increase of cycling number (Figure S6). The capacity retention of the plateaus is 70% and 60% for SnO_2/GeO_2 and SnO_2/G, respectively, indicating that the nano-sized GeO_2 indeed plays a critical role in the conversion reactions of Sn into SnO_2 and the decomposition of Li_2O.

In order to verify the above assumption, *ex-situ* XPS analysis was also carried on, as shown in Figure 7. The XPS spectra for $SnO_2(GeO_2)_{0.13}$/G electrodes was obtained after 100 discharge/charge cycles. For the initial sample, the peak came from the $SnO_2(GeO_2)_{0.13}$/G powder before making electrode. From the Figure 7a, the variety of Ge 3d from initial state to 0.01 V and then to 3.0 V could be obviously observed. After discharge to 0.01 V, there is only Ge metal in the electrode.[33] Even after being charged to 3.0 V, Ge metal is also the main part in the electrode. However, Sn 3d exhibited a big different variety in the three states. After discharge to 0.01 V, the peaks from SnO_2 became undetectable, which might be attributed to the increase in the SEI film thickness and the embedded $Li_{4.4}Sn$ in the amorphous Li_2O matrix.[44, 45] In

contrast, after electrochemical reactions, metallic Ge is formed instead of GeO_2 in the nanocomposites. The metallic Ge reacts with Li ions, which prevents the formation of amorphous Li_2O matrix on its surface. Thus, the XPS signal of Ge 3d could be detected. When the electrode was charged to 3.0 V, the peaks of SnO_2 are presented again. The variety of SnO_2 in the charge and discharge process is in accord with our assumption. Therefore, we can conclude that the Ge acts as catalytic role to promote the reaction of metal (Sn and Ge) to metal oxides (SnO_2 and GeO_2) in the electrochemical process. In addition, most of Ge can stay as metal instead of GeO_2, which may be attributed to the stability of Ge in this system.

3. Conclusion

In summary, high specific capacity and ultra-stable $SnO_2(GeO_2)_{0.13}$/G anode material for lithium-ion batteries was designed by a simple, single-step, facile hydrothermal method. The improved electrochemical performance was attributed to the catalytic effect of Ge to enable the reversible reaction of metal (Sn and Ge) to metal oxides (SnO_2 and GeO_2) during the charging process. This novel design of high-performance nanocomposite materials opens up a new direction in the development of next-generation anode material for LIBs and potentially other energy storage devices.

Supporting Information

Supporting Information is available from the Wiley Online Library or from the author.

Acknowledgments

This work is supported by SUTD grant ZJURES042011. CSIRO's Science Leadership Program and the Australian Research Council (ARC) are gratefully acknowledged. ZJH and KO thank the support from the ARC's DECRA and Future Fellowships.

Reference

1 J. M. Tarascon and M. Armand, *Nature,* 2001, **414**, 359-367.
2 V. Etacheri, R. Marom, R. Elazari, G. Salitra and D. Aurbach, *Energy Environ. Sci.,* 2011, **4**, 3243-3262.
3 B. Scrosati and J. Garche, *J. Power Sources,* 2010, **195**, 2419-2430.
4 C. Wang, H. Wu, Z. Chen, M. T. McDowell, Y. Cui and Z. Bao, *Nat. Chem.,* 2013, **5**, 1042-1048.
5 Z. W. Seh, W. Li, J. J. Cha, G. Zheng, Y. Yang, M. T. McDowell, P.-C. Hsu and Y. Cui, *Nat. Commun.,* 2013, **4**, 1331.
6 C. Liu, F. Li, L. P. Ma and H. M. Cheng, *Adv. Mater.,* 2010, **22**, E28.
7 M. T. McDowell, S. W. Lee, J. T. Harris, B. A. Korgel, C. Wang, W. D. Nix and Y. Cui, *Nano lett.,* 2013, **13**, 758-764.
8 Y. G. Zhu, J. Xie, G. S. Cao, T. J. Zhu and X. B. Zhao, *RSC Adv.,* 2013, **3**, 6787-6793.
9 Y.-G. Zhu, G.-S. Cao, J. Xie, T.-J. Zhu and X.-B. Zhao *Nanosci. Nanotechnol. Lett.,* 2012, **4**, 35-40.
10 P. Poizot, S. Laruelle, S. Grugeon, L. Dupont and J. M. Tarascon, *Nature,* 2000, **407**, 496-499.
11 X. W. Lou, D. Deng, J. Y. Lee, J. Feng and L. A. Archer, *Adv Mater.,* 2008, **20**, 258-262.
12 X. L. Wu, Y. G. Guo and L. J. Wan, *Chem. – Asian J.,* 2013, **8**, 1948-1958.
13 J. Luo, J. Liu, Z. Zeng, C. F. Ng, L. Ma, H. Zhang, J. Lin, Z. Shen and H. J. Fan, *Nano Lett.* 2013, **13**, 6136-6143.
14 M. Reddy, G. Subba Rao and B. Chowdari, *Chem. Rev.* 2013, **113**, 5364–5457.
15 I. A. Courtney and J. R. Dahn, *J. Electrochem. Soc.,*1997, **144**, 2045-2052.
16 J. S. Chen, Y. L. Cheah, Y. T. Chen, N. Jayaprakash, S. Madhavi, Y. H. Yang and X. W. Lou, *J. Phys. Chem. C,* 2009, **113**, 20504-20508.
17 J. Zhu, Z. Lu, S. T. Aruna, D. Aurbach and A. Gedanken, *Chem. Mater.,* 2000, **12**, 2557-2566.
18 J. Liu, Y. Li, X. Huang, R. Ding, Y. Hu, J. Jiang and L. Liao, *J. Mater. Chem.,* 2009, **19**, 1859-1864.
19 M. S. Park, G. X. Wang, Y. M. Kang, D. Wexler, S. X. Dou and H. K. Liu, *Angew. Chem.,* 2007, **119**, 764-767.
20 D.-W. Kim, I.-S. Hwang, S. J. Kwon, H.-Y. Kang, K.-S. Park, Y.-J. Choi, K.-J. Choi and J.-G. Park, *Nano lett.,* 2007, **7**, 3041-3045.
21 X. W. Lou, Y. Wang, C. Yuan, J. Y. Lee and L. A. Archer, *Adv. Mater.,* 2006, **18**, 2325-2329.
22 S. Han, B. Jang, T. Kim, S. M. Oh and T. Hyeon, *Adv. Funct. Mater.,* 2005, **15**, 1845-1850.
23 X. W. Lou, C. M. Li and L. A. Archer, *Adv. Mater .,*2009, **21**, 2536-2539.
24 L. Zhang, H. B. Wu, B. Liu and X. W. Lou, *Energy Environ. Sci.,* 2014, **7**, 1013-1017.
25 L. Wang, D. Wang, Z. Dong, F. Zhang and J. Jin, *Nano lett.* 2013, **13**, 1711-1716.
26 Z. Wen, Q. Wang, Q. Zhang and J. Li, *Adv. Funct. Mater.,* 2007, **17**, 2772-2778.
27 X. W. Lou, D. Deng, J. Y. Lee and L. A. Archer, , *Chem. Mater.,* 2008, **20**, 6562-6566.
28 S.-M. Paek, E. Yoo and I. Honma, *Nano Lett.,* 2008, **9**, 72-75.
29 N. Zhang, Q. Zhao, X. Han, J. Yang and J. Chen, *Nanoscale,* 2014, **6**, 2827-2832.
30 R. A. Huggins, *J. Power Sources,* 1999, **81**, 13-19.
31 Y. Y. Hu, Z. G. Liu, K. W. Nam, O. J. Borkiewicz, J. Cheng, X. Hua, M. T. Dunstan, X. Q. Yu, K. M. Wiaderek, L. S. Du, K. W. Chapman, P. J. Chupas, X. Q. Yang and C. P. Grey, *Nat. Mater.,* 2013, **12**, 1130-1136.
32 C. H. Kim, Y. S. Jung, K. T. Lee, J. H. Ku and S. M. Oh, *Electrochim. Acta,* 2009, **54**, 4371-4377.
33 K. H. Seng, M.-h. Park, Z. P. Guo, H. K. Liu and J. Cho, *Nano Lett.,* 2013, **13**, 1230-1236.
34 L. Tang, Y. Wang, Y. Li, H. Feng, J. Lu and J. Li, *Adv. Funct. Mater.,* 2009, **19**, 2782-2789.
35 X. Zhou, Z. Dai, S. Liu, J. Bao and Y.-G. Guo, *Adv Mater* 2014, n/a-n/a.
36 J. C. Lytle, H. Yan, N. S. Ergang, W. H. Smyrl and A. Stein, *J. Mater. Chem.* 2004, **14**, 1616-1622.

37 B. Liu, Z. P. Guo, G. Du, Y. Nuli, M. F. Hassan and D. Jia, *J. Power Sources,* 2010, **195**, 5382-5386.
38 G. Kilibarda, D. V. Szabo, S. Schlabach, V. Winkler, M. Bruns and T. Hanemann, *J. Power Sources,* 2013, **233**, 139-147.
39 D. N. Wang, J. L. Yang, J. Liu, X. F. Li, R. Y. Li, M. Cai, T. K. Sham and X. L. Sun, *J. Mater. Chem. A,* 2014, **2**, 2306-2312.
40 Y. Wang, Z. J. Han, S. F. Yu, R. R. Song, H. H. Song, K. K. Ostrikov and H. Y. Yang, *Carbon* 2013, **64**, 230-236.
41 C.-j. Liu, F.-h. Xue, H. Huang, X.-h. Yu, C.-j. Xie, M.-s. Shi, G.-z. Cao, Y.-g. Jung and X.-l. Dong, *Electrochim. Acta,* 2014, **129**, 93-99.
42 J. Zhang, R. Wang, X. Yang, W. Lu, X. Wu, X. Wang, H. Li and L. Chen, *Nano lett.,* 2012, **12**, 2153-2157.
43 L. Ding, S. He, S. Miao, M. R. Jorgensen, S. Leubner, C. Yan, S. G. Hickey, A. Eychmüller, J. Xu and O. G. Schmidt, *Sci. Rep.,* 2014, **4**, 4647
44 G. An, N. Na, X. Zhang, Z. Miao, S. Miao, K. Ding and Z. Liu, *Nanotechnology,* 2007, **18**, 435707.

45 Z. Chen, M. Zhou, Y. Cao, X. Ai, H. Yang and J. Liu, *Advanced Energy Materials*, 2012, **2**, 95-102.

Figure Caption

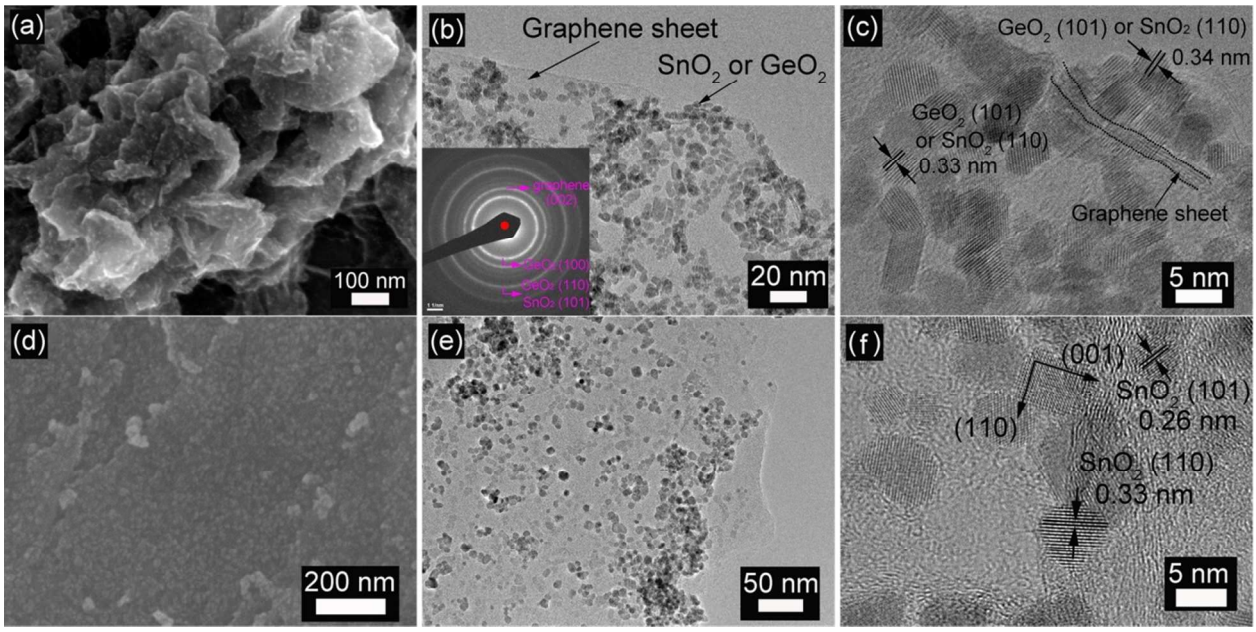

Figure 1. Structures of $SnO_2(GeO_2)_{0.13}$/G and SnO_2-G nanocomposites. (a) SEM and (b) TEM images of $SnO_2(GeO_2)_{0.13}$/G nanocomposite show the uniform distribution of nanoparticles on graphene sheets. Inset in (b) is the SAED pattern of $SnO_2(GeO_2)_{0.13}$/G nanocomposite. (c) High-resolution TEM image of $SnO_2(GeO_2)_{0.13}$/G indicates the lattice spacings of SnO_2 and GeO_2 nanoparticles. (d) SEM image of SnO_2/G nanocomposite. (e) Low- and (f) high-resolution TEM images of SnO_2 nanoparticles on graphene.

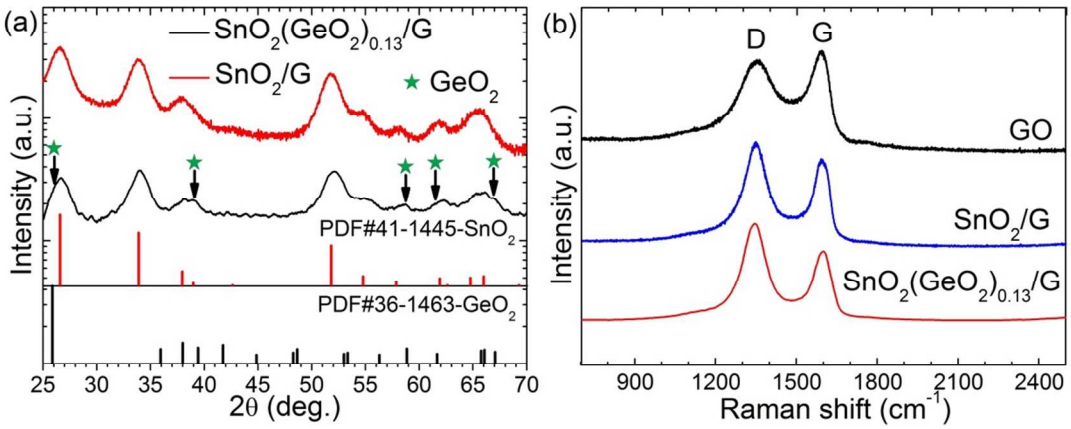

Figure 2. (a) X-ray diffraction (XRD) patterns of SnO_2/G and $SnO_2(GeO_2)_{0.13}$/G nanocomposites. The diffraction patterns of SnO_2 in both samples are indexed to the tetragonal structure of SnO_2 (JCPDS No. 41-1445) and the GeO_2 in $SnO_2(GeO_2)_{0.13}$/G is indexed to the hexagonal structure of GeO_2 (JCPDS No. 36-1463). (b) Raman spectra of graphene oxide (GO), SnO_2/G and $SnO_2(GeO_2)_{0.13}$/G with the labeled D and G bands of carbon.

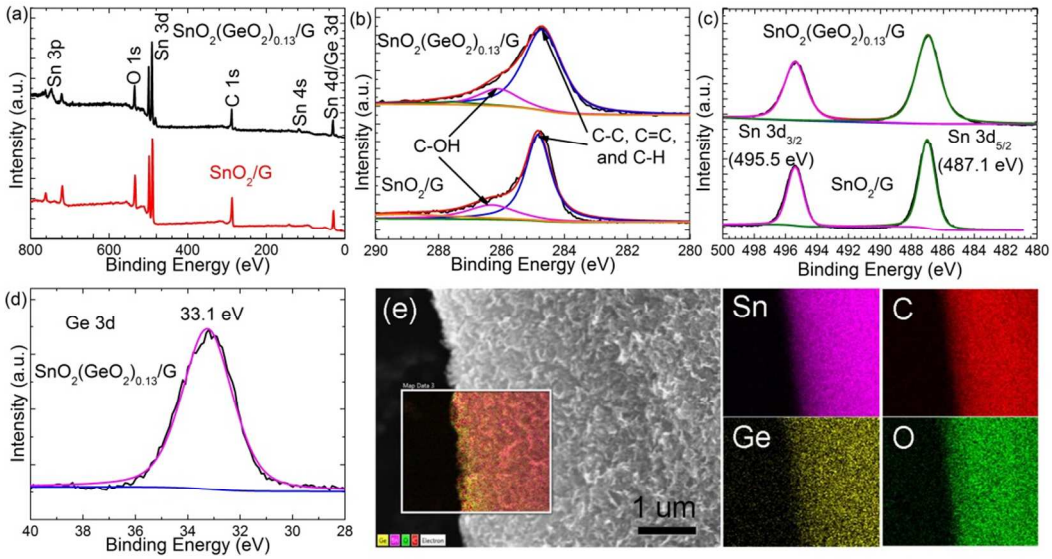

Figure 3. (a) XPS wide-scan spectra of $SnO_2(GeO_2)_{0.13}$/G and SnO_2/G nanocomposites; (b) C 1s and (c) Sn 3d spectra of $SnO_2(GeO_2)_{0.13}$/G and SnO_2/G nanocomposites (d) Ge 3d spectrum of $SnO_2(GeO_2)_{0.13}$/G; (e) SEM image of $SnO_2(GeO_2)_{0.13}$/G and the Sn, C, Ge, and O element mapping images of the squared area, which show the uniform distribution of the four elements.

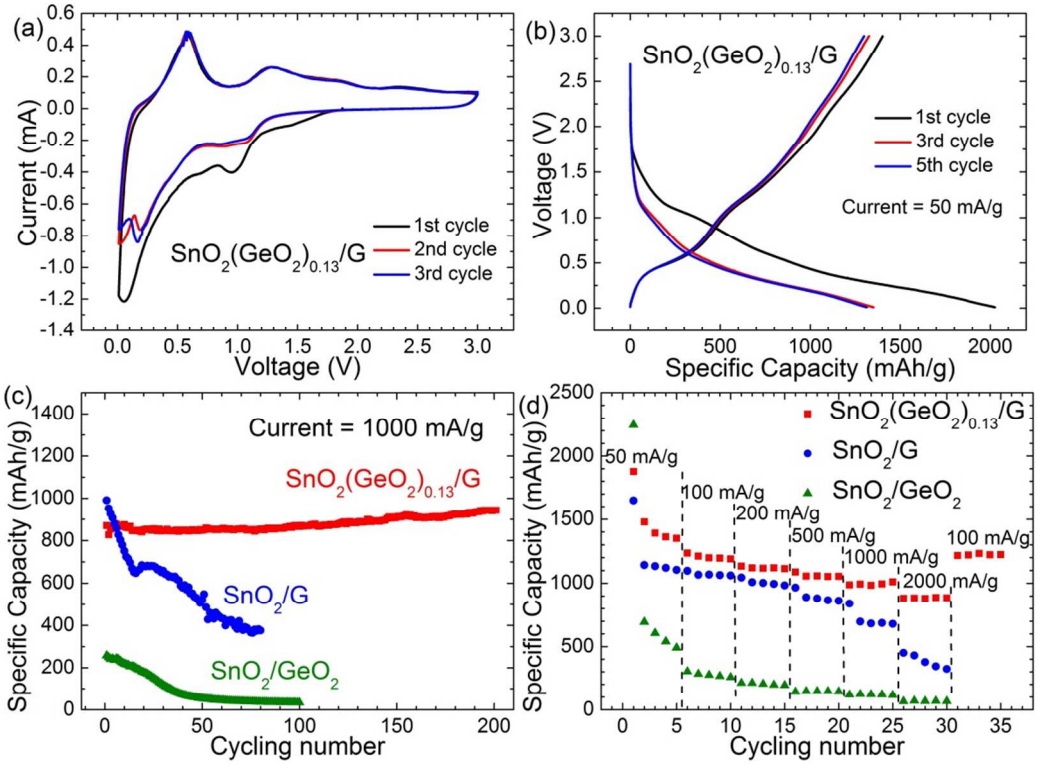

Figure 4. Electrochemical performance of the nanocomposites. (a) CV curves of the first three cycles of $SnO_2(GeO_2)_{0.13}$/G electrode; (b) Galvanostatic charge/discharge profiles of 1st, 3rd, and 5th cycle of the $SnO_2(GeO_2)_{0.13}$/G electrode; (c) the comparison of cycling stability for $SnO_2(GeO_2)_{0.13}$/G, SnO_2/G, and SnO_2/GeO_2; (d) Rate capability of the three materials.

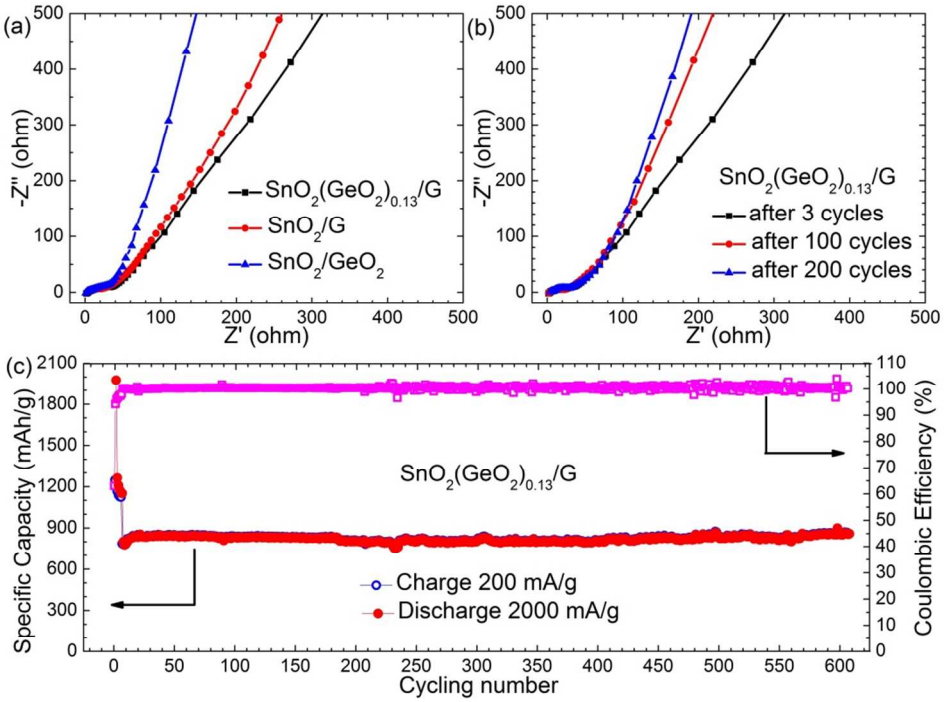

Figure 5. (a) Electrochemcial impedance spectroscopy (EIS) spectra of $SnO_2(GeO_2)_{0.13}$/G, SnO_2/G, and SnO_2/GeO_2. (b) EIS of $SnO_2(GeO_2)_{0.13}$/G after 3, 100, 200 cycles. (c) Cycling stability and Coulombic efficiency of the $SnO_2(GeO_2)_{0.13}$/G up to 600 cycles.

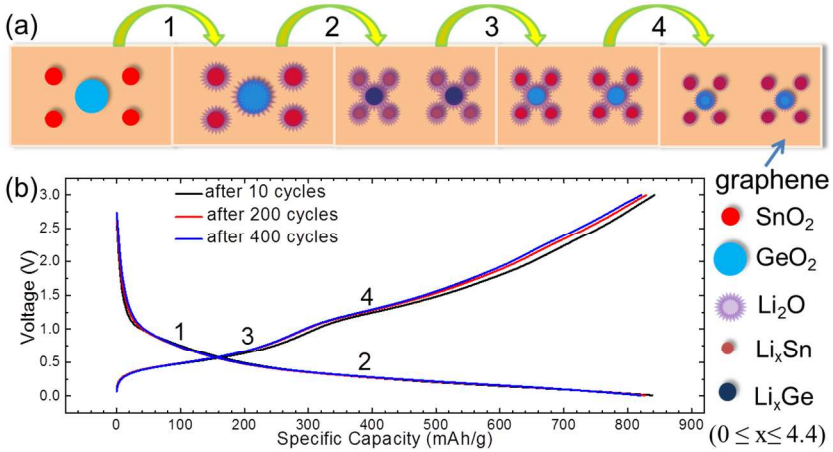

Figure 6. (a) The schematic diagram showing the reaction mechanism of $SnO_2(GeO_2)_{0.13}$/G nanocomposites. Step 1 is the process of SnO_2 and GeO_2 reacting with Li^+ to form Sn and Ge metal nanoparticles, which are covered by Li_2O. Step 2 is the lithiation process of Sn and Ge with the Li ions. Step 3 is the dealloying process of Li_xSn or Li_xGe ($0 \le x \le 4.4$). Step 4 is the reaction of Sn and Ge metal nanoparticles with Li_2O to form SnO_2 or GeO_2. The four reaction steps are corresponding to four platforms in the charge and discharge curves as shown in (b).

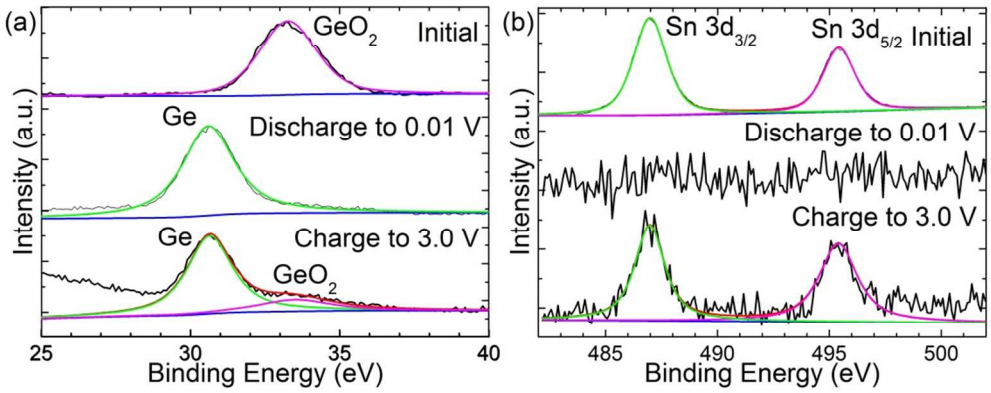

Figure 7. Ex-situ XPS spectroscopy analysis of the $SnO_2(GeO_2)_{0.13}$/G composite after 100 charge and discharge cycles: (a) Ge 3d spectra from the initial state to 0.01 V and then to 3.0 V. After discharging to 0.01 V, Ge is detected; (b) Sn 3d spectra from the initial state to 0.01 V and then to 3.0 V.

TOC

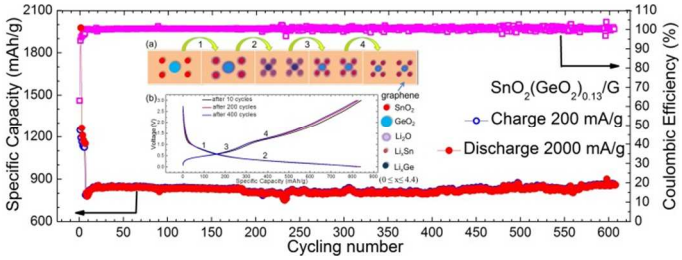

The design of $SnO_2(GeO_2)_{0.13}$/G composition provides a new avenue to improve the specific capacity and stability of SnO_2. The catalytic role of Ge promotes the reversible electrochemical reaction from SnO_2 to Sn, overcoming the limitation of traditional specific capacity of SnO_2. The introduction of graphene not only stabilizes the structure of the composition but also keeps the catalyst active after long cycles. As such, the $SnO_2(GeO_2)_{0.13}$/G nanocomposites demonstrate a retention rate of almost 100% after 600 cycles.